Supplementary Information: Forces, kinetics, and fusion efficiency altered by the full–length synaptotagmin-1 – PI(4,5)P$_2$ interaction in constrained geometries

Joern Dietz,[†] Marieelen Oelkers,[†] Raphael Hubrich,[‡] Angel Pérez-Lara,[¶] Reinhard Jahn,[¶] Claudia Steinem,[*,‡] and Andreas Janshoff[*,†]

[†]*Georg-August Universität, Institute for Physical Chemistry, Tammannstr. 6, 37077 Göttingen, Germany*

[‡]*Georg-August Universität, Institute for Organic and Biomolecular Chemistry, Tammannstr. 2, 37077 Göttingen, Germany*

[¶]*Department of Neurobiology, Max Planck Institute for Biophysical Chemistry, Am Faßberg 11, 37077 Göttingen, Germany.*

E-mail: csteine@gwdg.de; ajansho@gwdg.de

Supplementary Data

Syt-1-membrane interactions monitored by TPM measurements.

Two opposing supports, silica beads serving as Brownian particles and a planar glassy surface, were separately coated with continuous bilayers via vesicle spreading. Subsequently, the membrane-coated beads were gently added to the planar bilayer via a flow chamber in order to establish physical contact. The suspended particles adhere against buoyancy and thermal fluctuation, and eventually, temporal binding might occur between the two opposing membranes leading to restricted Brownian motion depending on the experimental conditions. Example trajectories in the absence and presence of syt-1 are shown in Fig. SI 1. From holographic patterns, we can read out individual trajectories of a particle during video microscopy. This allowed us to identify impaired Brownian motion due to the presence of an attractive potential and eventually strong restriction in response to specific non-covalent tethering. Fig. 1B-D shows the typical workflow starting from recording Brownian motion to the mean square displacement (MSD) after a principal component analysis. The MSD analysis then provides direct information about the diffusion constant and the confinement radius. The color of the individual MSD curves refers to a categorization rationalized by the progression of conceivable scenarios after sedimentation of the membrane-coated beads (Fig. SI 2 and Fig. SI 11). The shape of the projected trajectory provides insight to what extent multiple attachment points are present, i.e., deviations from a circular towards elliptical distributions are an indication that more than one attachment point is present (Fig. SI 3).[1,2]

The accuracy of x-position determination was about 1.4 nm, that of the y-position determination was about 1.6 nm, at an acquisition rate of 200 fps. Immobile silica microspheres ($R = 480$ nm) to determine the practical resolution limit were adhered non-specifically to the flow cell surface. For mechanical drift correction, a reference microsphere was tracked simultaneously, and its position was subtracted. The standard deviations of the position

distributions for membrane coated silica microspheres fused to the surface are $\sigma_x = 3.04$ nm and $\sigma_y = 2.65$ nm, respectively.
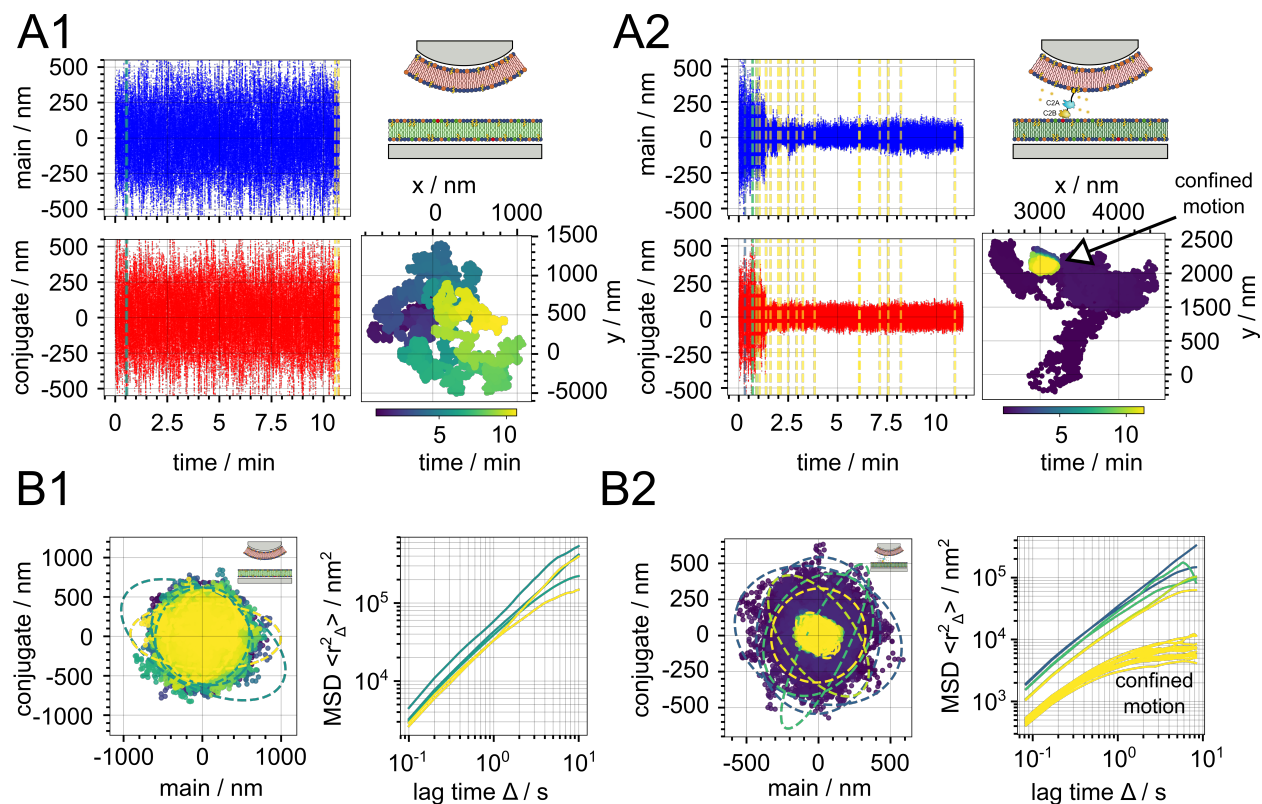
Fig. SI 1: Individual particle motion trajectories in the absence (1) and in the presence (2) of syt-1, respectively. **A1** Motion data of the particle position onto the x- or y-plane parallel to the substrate after applying a principle component analysis (PCA), along with a schematic illustration of the experiment and the particle trajectory in the absence of syt-1. **A2** Motion data of the particle position onto the x- or y-plane parallel to the substrate after applying a principle component analysis (PCA), along with a schematic illustration of the experiment and the particle trajectory in the presence of syt-1. Confined motion occurs at the end of the experiment as indicated. **B1** Trajectories and MSD analysis after PCA of weakly adhering beads in the absence of syt-1. **B2** Trajectories and MSD analysis of beads in the presence of syt-1. The color code relates to our categorization further detailed in Fig. SI 2 and SI 11.
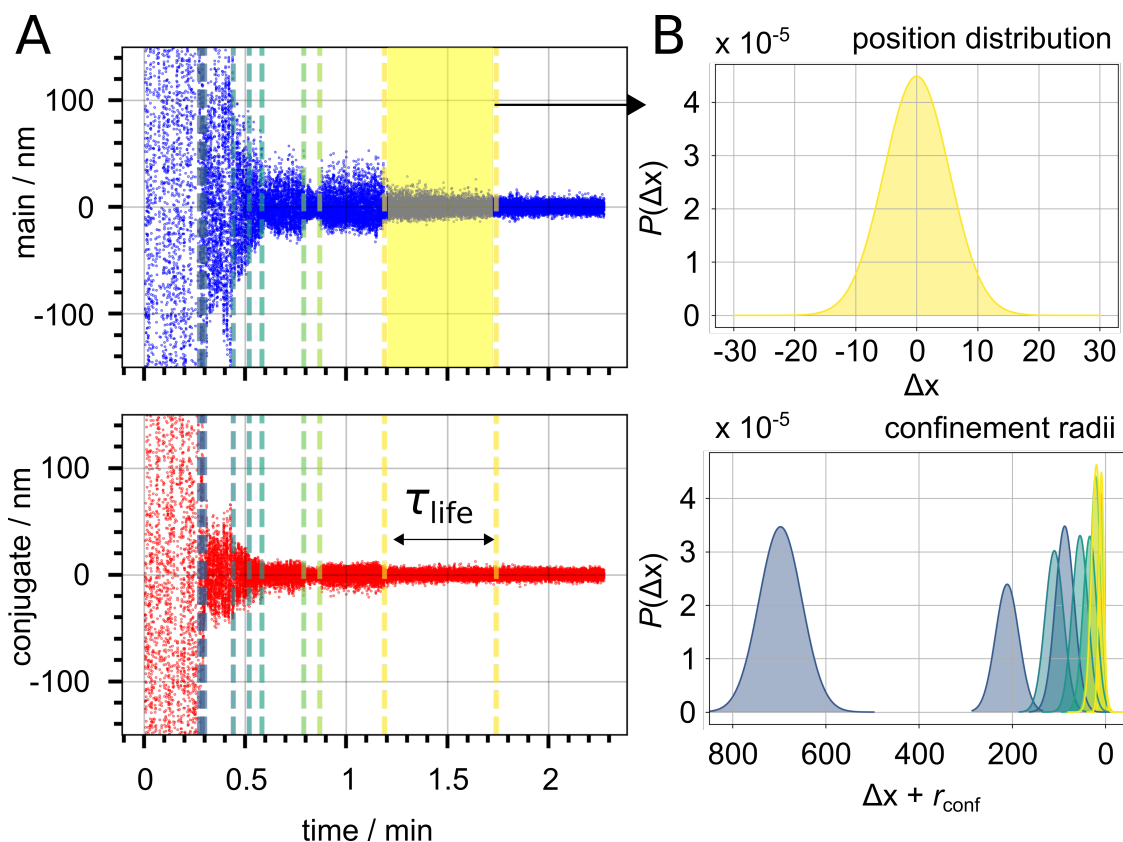
Fig. SI 2: Illustration of a time-resolved segmented tethered particle motion experiment and determination of confinement radii. **A** Motion data of the particle position onto the *x*- or *y*-plane parallel to the substrate after applying a PCA. **B** Motion corresponding to the position of the particle at different states as function of time from which a state's lifetime τ_{life} can be obtained. Gaussian distributions obtained from motion data related to the corresponding state defined by the confinement radius. Time-resolved and color coded confinement radii and motion data over a time course of 2 min, recorded with 200 fps.

Potential number of syt-1 molecules in the contact zone.

For TPM measurements a protein-to-lipid ratio (p/l) 1:1000 was reconstituted into host membranes covering the beads. The contact radius a of the bead (bead radius $R = 480\,\text{nm}$) with the target membrane is estimated from Hertzian mechanics:

$$a^3 = \frac{3FR}{4E}, \tag{1}$$

with F the contact force (100 pN), E the Young's modulus of the bilayer (≈ 10 MPa). The contact area $A_{\text{con}} = \pi a^2$ between the membrane-covered bead and the planar target membrane amounts to $A_{\text{con}} \approx 700$ nm^2. Typically, a phospholipid occupies an area of 0.7 nm^2. Thus, there is ≈ 1 syt-1 molecule to be found in the contact area. However, in the time course of the experiments, we observe that two and sometimes even more contacts are established leading to very strong constriction of the Brownian movement (Fig. SI 1, Fig. SI 2).

In the case of colloidal microscopy, we use a higher p/l ratio 1:100 in order to obtain enough events within one force map.[1]

Categorization of Brownian trajectories from TPM measurements.

Fig. SI 2, SI 3 exemplarily show the raw data (Brownian trajectories) after principal component analysis and illustrates the categorization (color coded) based on discrete steps towards stronger confinement.

Fig. SI 4 shows how the presence of syt-1 alters the confined motion of membrane-coated beads on a target membrane with different composition.

---

[1]Finite roughness of the bead's surface might lead to even smaller contact areas.
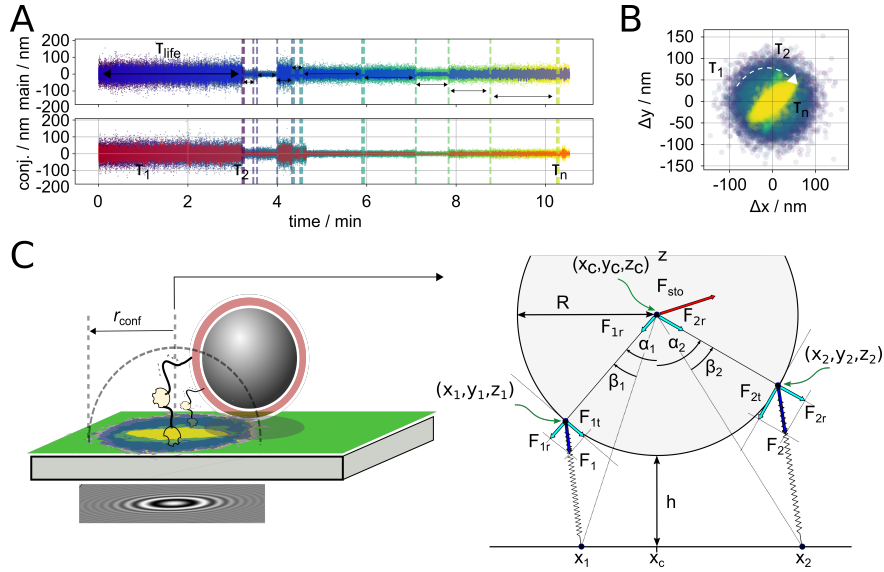
Fig. SI 3: Analysis of motion data (time-traces) exhibiting switching activity from single to multiple syt-1 bonds to the target membrane. **A** Motion data of the particle position onto the x- or y-plane parallel to the substrate after applying PCA, where r_{conf} switches between bound and unbound states with a lifetime of τ_{life} (τ_n: 1,2,.. n). Switching of states are discrete (dotted lines) and the elapsed time period between two consecutive events corresponds to a single-state lifetime of bound tethers. **B** The corresponding 2D position (Δx, Δy) of the bead shown in the same colors as in A. **C** Illustration of a segmented tethered particle motion experiment with a secondary bond restricting the particle to an elliptic motion pattern conceptualizing a bead exposed to lateral forces, torques, and viscous friction. Protein tethers are modeled as springs attached to the bead and the substrate at fixed anchor points. $\vec{P_1}$ and $\vec{P_2}$ on the bead, $(x_1, 0, 0)$ and $(x_2, 0, 0)$ on the substrate.
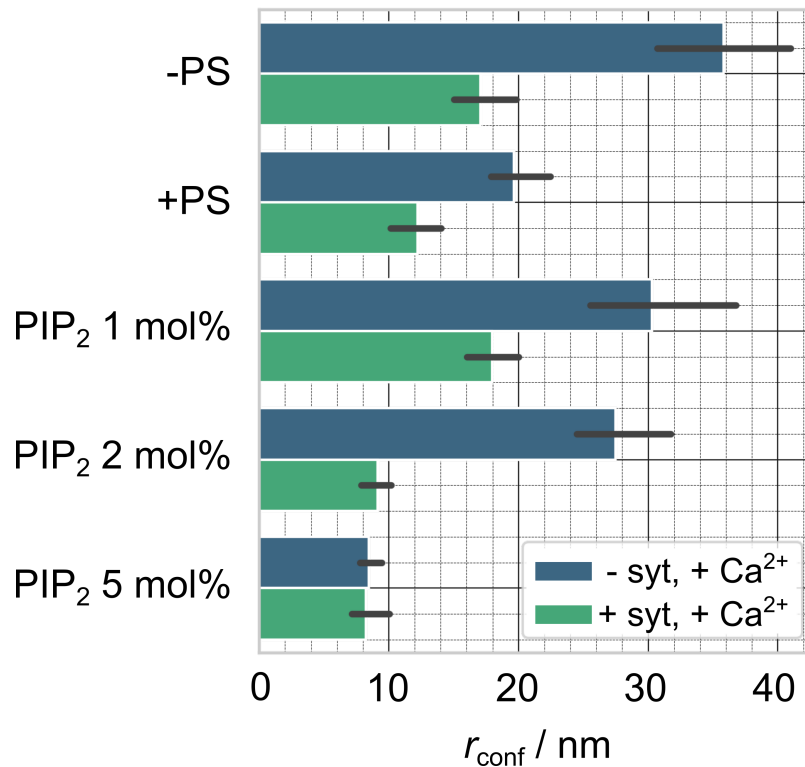
Fig. SI 4: Influence of the presence of syt-1 on confined motion of membrane-coated beads on a target membrane with different composition. Median estimator of confinement radii from TPM experiments against different membranes in the presence and absence of syt-1, while calcium ions are in solution. Results are grouped by composition of target membranes: (DOPC:POPE:POPS:Chol:PI(4,5)P$_2$:Atto488-DPPE 50:29:0:20:0:1 (-PS), 50:19:10:20:0:1 (+PS), 50-x:19:10:20:x:1 (PIP$_2$, with $x = 1$ mol%, 2 mol%, 5 mol%)). Error bars indicate confidence intervals of 95 % drawn around estimated values.

Syt-1-membrane interactions monitored by colloidal probe microscopy.

CPM permits precisely measuring adhesion forces between two surfaces due to a small but defined contact zone connected by a soft spring. Previously, CPM has been successfully used to study membrane-membrane interactions including fusion mediated by SNAREs.[3–5] Only limited by thermal noise, force resolution is down to a few Piconewtons allowing to even examine molecular events such as protein unfolding.

To ensure that individual single molecule rupture events are collected we limited the $PI(4,5)P_2$ content in the CPM experiments to 1 mol%. Experiments were performed in absence (1 mM EDTA) or presence (1 mM $CaCl_2$) of Ca^{2+}. Pulling velocity was adjusted between 100 - 1000 nm/s and dwell times between 3-10 s to provide enough time to form specific bonds. To investigate the role of $PI(4,5)P_2$, membranes lacking $PI(4,5)P_2$ were prepared as control, in which $PI(4,5)P_2$ was replaced by PS to preserve the amount of negatively charged lipids in the target membrane. Alternatively, we also removed PS from the target membrane replacing it with PC to examine the isolated impact of $PI(4,5)P_2$ on the interaction with syt-1. Notably, not all individual force curves show all three steps in the presence of syt-1, $PI(4,5)P_2$ and PS. Sometimes the contact is prematurely lost midways, but most force curves show two to three discernible events (Fig. 3A (inset)) as indicated. Contrary, some force curves display the extrusion of membrane tethers with long-reaching plateaus (up to 140 nm) at approximately 40 pN. Since the adhesion energy to the surface is around 0.1 mN/m, we expect to measure tether forces around 40 pN. Our experiments also gather rupture forces exceeding 100 pN at larger distances than 60 nm indicative of unfolding the C2B domain, but these occur far less frequently. In our analysis we discarded events that could clearly be assigned to multiple protein tethers formed in the contact zone. In this case, forces to separate the two surfaces exceeded 200-300 pN and extended several hundreds of nanometers away from the surface indicative of lifting off the membrane from the surface. Considering that approximately 10-100 syt-1 molecules might be found

in the contact zone these events can occur frequently. As mentioned earlier, the number of molecular contacts formed in the contact zone depends strongly on the microscopic roughness of the probes (beads and surfaces), so the amount of reconstituted syt-1 must be adjusted to obtain predominantly single-molecule break events.

CPM - control experiments.

Fig. SI 5 shows averaged force distance curves obtained from three different experiments, each comprising a large number of force curves from different force volume maps ($n > 1000$ force curves). The red curve represents the experiment shown in the main text in the presence of Ca^{2+} (Fig. 3). The planar target membrane contains PS and PI(4,5)P$_2$, while the membrane on the colloidal probe is composed of PC with reconstituted syt-1. The purple curve depicts the averaged force distance curve obtained for the bilayer separation with the same lipid composition but in the absence of syt-1 and Ca^{2+}, while the green curve is the result obtained for the same conditions but in the presence of Ca^{2+}. Interestingly, we find that the non-specific interactions between membranes in the absence of syt-1 are strongly enhanced in the presence of Ca^{2+}. However, in agreement with our interpretation, we do not observe rupture events assigned to unfolding of the C2A domain or to the last separation step at approximately 60 nm assigned to C2B attached to PI(4,5)P$_2$ (red curve in Fig. SI 5).

Fig. SI 6 shows the impact of Ca^{2+} on averaged force distance curves obtained from separating two membranes in the presence of syt-1. In the absence of Ca^{2+} interaction forces are generally diminished and the last rupture event, assigned to the PI(4,5)P$_2$-syt-1 interaction, is moved substantially closer to the contact point, which indicates that forces in the absence of Ca^{2+} are too small to enforce unfolding of the C2A domain with appreciable probability. Interestingly, the PI(4,5)P$_2$-C2B interaction did not vanish entirely but is diminished by a factor of 1.5.
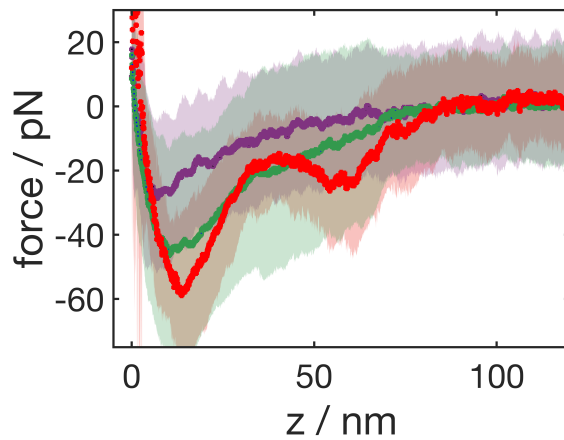
Fig. SI 5: CPM control experiments in the absence of syt-1. The green curve is the averaged force distance curve of CPM experiments employing two neat bilayers (CPM: DOPC:BODIPY, 99:1; planar bilayer: DOPC:DOPS:PI(4,5)P_2:Texas-Red-DHPE, 87:11:1:1) in the presence of Ca^{2+} (1 mM, $n = 74$), while the purple curve represents experiments of the same bilayers in the absence of Ca^{2+} (1 mM EDTA, $n = 74$). For comparison, the red curve from Fig. 4 (main text) represents averaged force distance curves of syt-1-functionalized membranes (p/l = 1:100) separated from planar bilayers in the presence of PS and PI(4,5)P_2 and Ca^{2+} (1 mM, $n = 56$). Pulling velocity was set to 1000 nm/s for all experiments and dwell time in contact was in between 3-10 s.
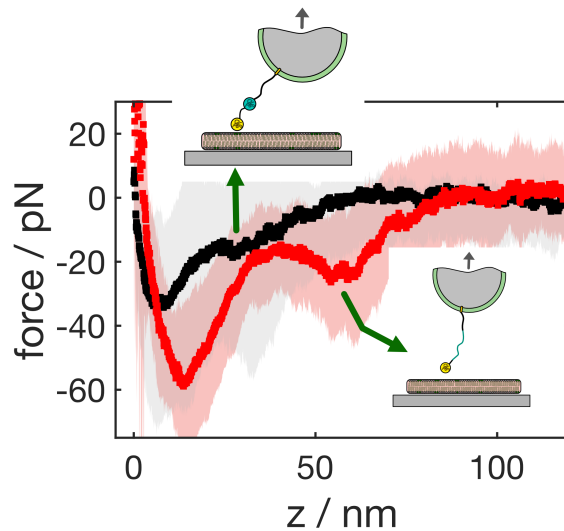
Fig. SI 6: Averaged force distance curves obtained from separating colloidal membrane probes equipped with syt-1 from planar target membranes containing both PS and PI(4,5)P_2 in the presence of Ca^{2+} (red, 1 mM Ca^{2+}, $n = 56$) and in the absence (black, 1 mM EDTA, $n = 93$). Pulling velocity was set to 1000 nm/s and dwell time in contact was in between 3-10 s.

Fig. SI 7 shows averaged forces obtained at pulling speeds of 500 nm/s and 1000 nm/s, respectively. As typical for conventional slip bonds, we find an increase in rupture forces with speed. Pulling velocities are, however, practically limited by hydrodynamic forces. Albeit colloidal particles have many advantages over conventional AFM tips, hydrodynamic forces become already appreciable at pulling velocities exceeding 1000 nm/s. I.e., at 1000 nm/s the hydrodynamic drag force is around 10 pN. At pulling speeds as large as 5000 nm/s, the drag forces generate pseudo adhesion forces that exceed any molecular interactions.[6] As a consequence, we refrained from higher rates than 1000 nm/s to limit the impact of hydrodynamic drag.
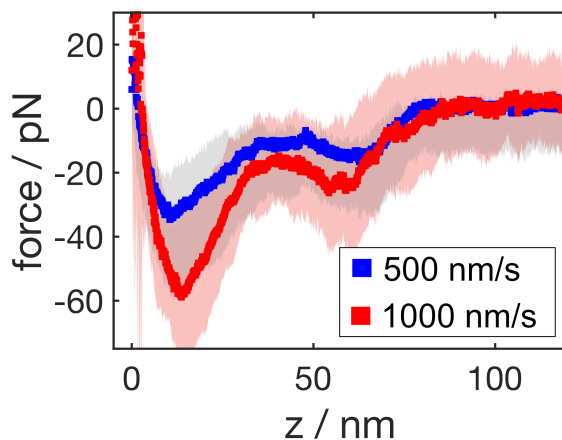
Fig. SI 7: Averaged force distance curves obtained from separating colloidal membrane probes equipped with syt-1 from planar target membranes containing both PS and PI(4,5)P$_2$ in the presence of Ca^{2+} at two different pulling velocities. Dwell time in contact was in between 3-10 s ($n = 91$ for 500 nm/s and $n = 56$ for 1000 nm/s).

CPM - free energy reconstruction.

Based on Jarzynski's relation[7] of the free energy difference G and the non-equilibrium work W to shuttle between two states in numerous paths, Hummer and Szabo provided an approximation for stiff cantilevers to calculate free-energy profiles along mechanical reaction coordinates obtained from single molecule pulling experiments.[8] The free energy $G(z_{TS})$ as a function of tip-sample distance $z_{TS} = vt - z_c$ is obtained from:

11

$$G(z_{TS}) = \int_0^{z_{TS}} dz_{TS} \frac{\left\langle F(z_{TS})e^{-\beta W(z_{TS})}\right\rangle}{\left\langle e^{-\beta W(z_{TS})}\right\rangle},$$ (2)

with the restoring force $F = k_c z_c = k_c(vt - z_{TS})$, the spring constant of the cantilever k_c, $\beta = (k_B T)^{-1}$, z_c the cantilever deflection, v the piezo velocity, $V(z_{TS}(0))$ the potential at the contact point at time zero, and the $W(z_{TS})$, the integral under each force curve:

$$W(z_{TS}) = \int_0^{z_{TS}} F dz'_{TS} + \frac{1}{2}k_c \left(\frac{F}{k_c}\right)^2 - V(z_{TS}(0))$$ (3)

Fig. SI 8 shows a typical free energy reconstruction from an ensemble of force curves obtained far from equilibrium. We found that the last separation event associated with the C2B domain unbinding from PI(4,5)P$_2$ requires a free energy input of about $14 \pm 2\,k_B T$ ($n = 3$). The largest energy contribution (almost $40\,k_B T$) comes from the concerted action involving the calcium bridged bilayer-bilayer interaction and the cooperative binding of the two C2 domains leading to unfolding of the C2A domain.
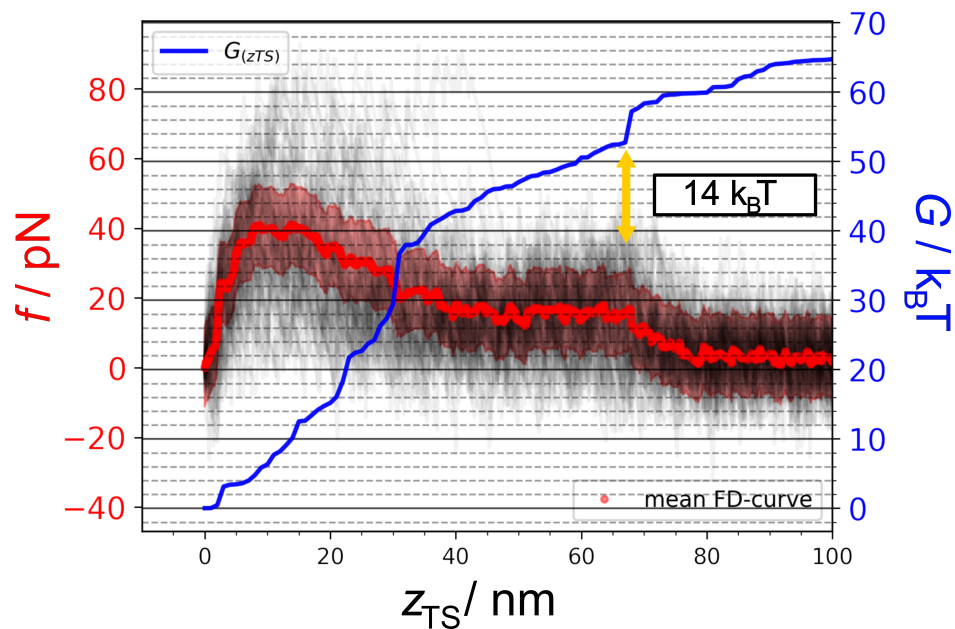
Fig. SI 8: Reconstruction of the free energy profile $G(z_{TS})$ from an ensemble of 81 single unfolding force curves (black) obtained by separating colloidal membrane-coated probes equipped with syt-1 from planar target membranes containing both PS and PI(4,5)P_2 in the presence of Ca^{2+} (1 mM) and recorded at 500 nm/s. The averaged force distance curve is shown in red. The separation of the C2B domain from the target membrane was associated with a free energy change of about 14 $k_B T$.

Membrane fusion monitored by TPM measurements.

The bead membrane as well as the planar target membrane were equipped with SNAREs. Full-length synaptobrevin 2 (syb 2) was reconstituted in the membrane covering the colloidal beads and the ΔN49-complex composed of syntaxin 1A, SNAP-25 and the soluble synaptobrevin 2 fragment (aa 49–96) were reconstituted into the planar membrane.
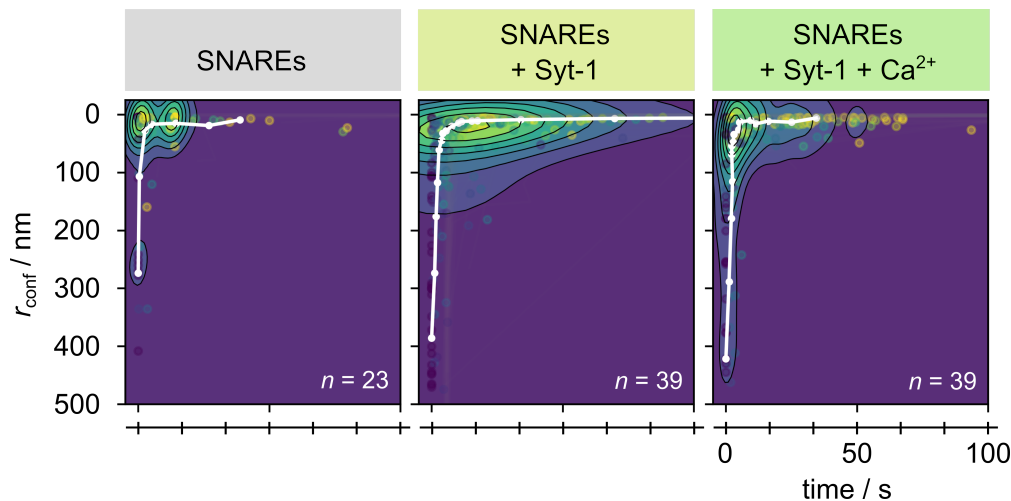
Fig. SI 9: Contour plots of the confinement radii r_{conf} as a function of time over a period of 100 s obtained from trajectories of membrane-coated beads (DOPC/POPE/Chol/TexasRed-DPPE) doped with either only synaptobrevin 2 (syb 2, p/l = 1:500) or syb 2 (p/l = 1:500) and syt-1 (p/l = 1:1000) and in the presence of Ca^{2+} after contact with planar target membranes composed of DOPC/POPE/POPS/Chol/PI(4,5)P$_2$/Atto488-DPPE (48:19:10:20:2:1) and doped with the ΔN49-complex (p/l = 1:500). The median trajectory is shown in white.

The median trajectory of the confinement radii in the presence of SNAREs is larger than those found in the absence of SNAREs, which might be attributed to the overall larger protein content in the bead and planar target membrane, respectively (Fig. SI 9). The presence of bulky protein domains in the contact zone prohibits close contact. However, after the first contact, the confinement radius quickly decreases down to the resolution limit of a few nanometers indicating close contact of the two membranes or even merging of the two membranes as expected for the fusion process to occur. To elucidate whether fusion has occurred, we took advantage of the two fluorophors in the opposing membranes. Upon fusion of the two membranes, we observed lipid mixing in dual color fluorescence micro-

graphs supporting the notion that fusion occurs in the presence of SNAREs (Fig. SI 10). The trajectories do not significantly change upon addition of syt-1 in the absence and presence of Ca^{2+} demonstrating that the SNAREs themselves already tether the bead membrane to the target membrane.
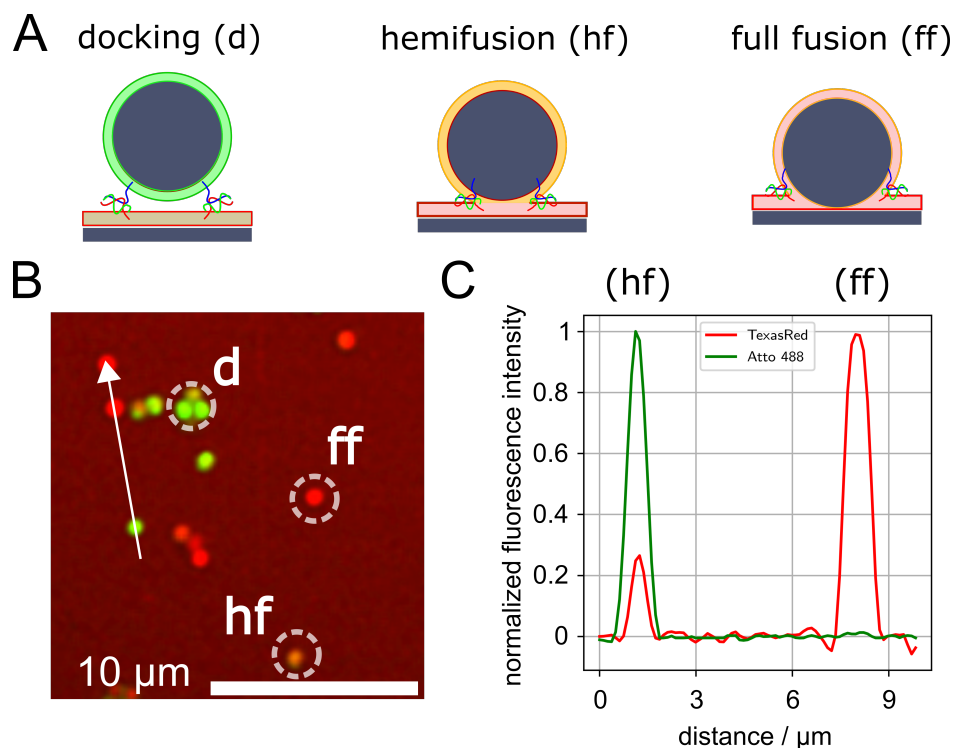
Fig. SI 10: **A** Schematic illustration of membrane-coated colloidal beads during the fusion process in the presence of SNAREs. Membranes come into close proximity tethered via SNAREs (docking, d) before hemifusion (hf) and full-fusion (ff) occurs. **B** Dual-channel fluorescence image demonstrating the merging of the outer membrane leaflets (orange, hf) and both leaflets (red, ff) after docking (green). Scale bar: 10 μm. **C** Normalized fluorescence intensity profile of two beads acquired along the white line (direction given by the arrow) shown in **B**. Hemifusion (hf) is identified by a relative intensity ratio of the supported dye I_{Rel} smaller than 0.5 as expected when only the outer leaflets merge, while full fusion (ff) of both leaflet leads to a relative intensity of $I_{Rel} \approx 1$.

From TPM, we have gathered the range of motion of restricted movements. This is confirmed by Visser et al.,[1,2] who recently demonstrated that the motion patterns of molecularly tethered particles are susceptible to the molecular system, binding the particle to the substrate, and the morphology near the molecular attachment point in the context of membrane fusion. In conclusion, it is important to relate restricted Brownian motion

15

to the actual distance between the membranes. We intuitively assume that smaller gaps between membranes lead to more friction and more hydrodynamic interaction between the particles and the substrate. In conventional TPM studies employing linear tethers, it is possible to establish a well-defined relation between the tether length and the magnitude of Brownian fluctuations of the bead and use this as a calibration curve. Furthermore, tethered particles can show a large variety of motion patterns. For example, double molecular tethering leads to stripe-shaped motion patterns, which we also frequently observe. Fig. SI 11 shows how we envision the entire process of merging of bilayers starting from free Brownian movement of the particle to initial contact via electrostatic interactions, over syt-1 confinement (tethering), followed by SNARE zippering (docking) and eventually to membrane fusion.

We infer this categorization from observation of discrete steps in confinement found in particle trajectories that eventually lead to full fusion as confirmed by fluorescence microscopy of the beads (Fig. SI 10). Notably, these are not always sharp transitions between the different states, leading to some uncertainty in this categorization, nonetheless serving as an orientation to how the process develops over time.
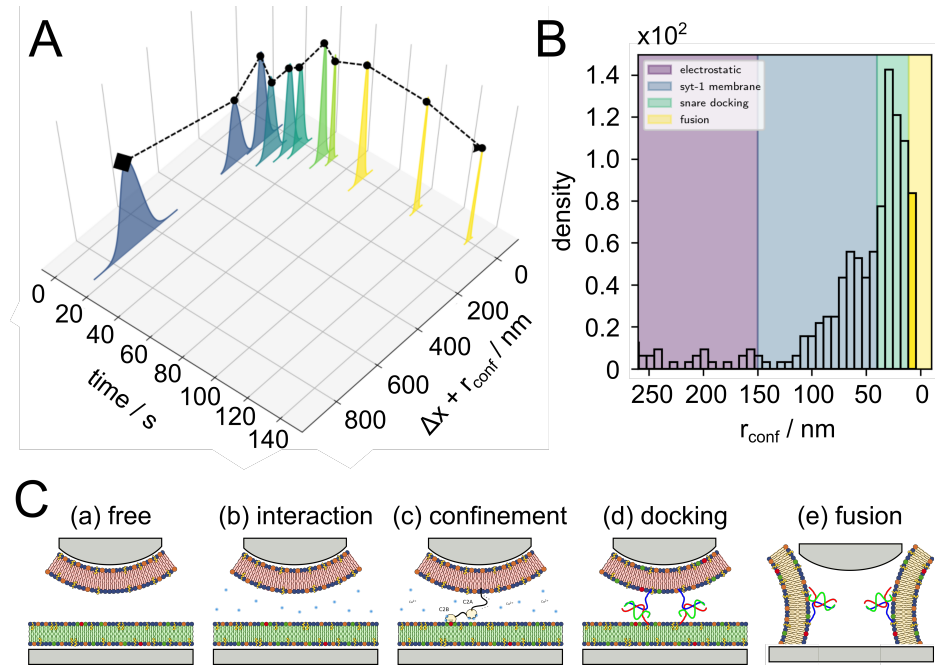
Fig. SI 11: Illustrative construction of a single membrane fusion landscape from time-resolved confinement states. **A** Time-resolved trajectory of a bead with reconstituted syb 2 (p/l = 1:500) and syt-1 (p/l = 1:1000) (black curve). Gaussian distributions of the beads movement from its displacement are centered on its respective radius of confinement $\Delta x + r_{\text{conf}}$. **B** Color coded histogram of confinement radii related to their confinement state. **C** Possible interactions between the probe and the planar membrane. (a) Free Brownian movement without interaction with the planar membrane. (b) The probe attaches to the target membrane and moves in confined space. (c) The probe attaches to the planar membrane through a syt-1 tether with $r_{\text{conf, syt}} < r_{\text{conf, EI}}$ (EI: electrostatic interaction). (d) Decreased confinement radius in which SNARE docking can happen; $r_{\text{conf, docking}} < r_{\text{conf, syt}}$. (e) Confinement radii where membrane fusion occurs $r_{\text{conf, fusion}} < 11$ nm.

Membrane fusion kinetics monitored on pore-spanning membranes.
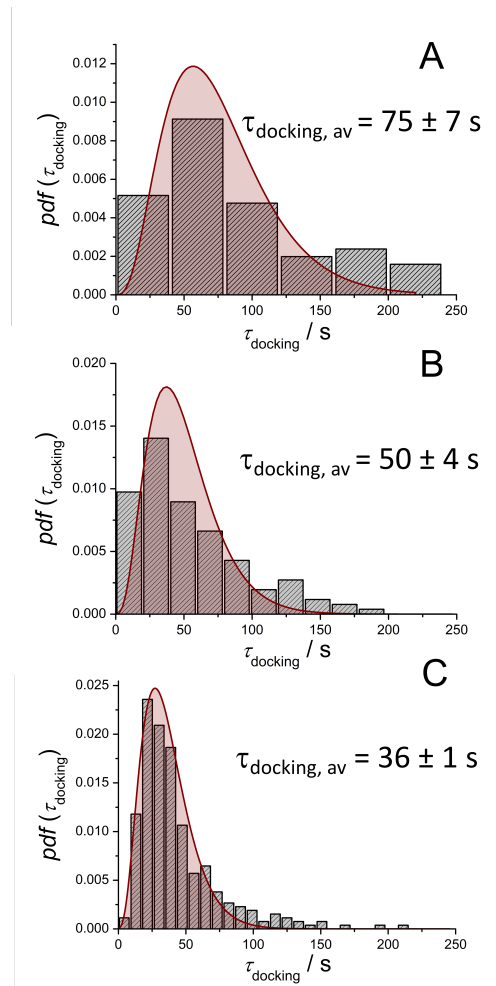
Fig. SI 12: Histograms of the delay times τ_{docking} between docking and fusion and the corresponding fit to the data with $N = 4$ (solid lines). Proteo-LUVs composed of DOPC/POPE/POPS/Chol/TexasRed-DPPE (50:19:10:20:1) doped with syb 2 (p/l = 1:500) and syt-1 (p/l = 1:1000) were added to PSMs composed of DOPC/POPE/POPS/Chol/PI(4,5)P$_2$/Atto-488 DPPE (48:19:10:20:2:1) doped with the ΔN49-complex (p/l = 1:500). **A** 0 μM CaCl$_2$, 0 mM ATP, $n = 65$, $m = 6$; **B** 100 μM CaCl$_2$, 0 mM ATP, $n = 130$, $m = 5$; **C** 100 μM CaCl$_2$, 5 mM ATP, $n = 305$, $m = 3$.

Fusion efficiency as a function of PIP$_2$

The Floyd model[9] was used to evaluate the kinetics data. In this model, the rate-limiting step from the docked state towards the fused state is not a single, one-step transition but a series of N transitions between the initial and the final state with a single rate constant k_1

for each transition leading to:

$$pdf\left(\tau_{\text{docking}}\right) = \frac{k_1^N \tau_{\text{docking}}^{N-1}}{\Gamma(N)} \exp\left\{-k_1 \tau_{\text{docking}}\right\} \tag{4}$$

with $\Gamma(N) = \int_0^\infty x^{N-1} e^{-x} \mathrm{d}x$ being the Gamma function. The Floyd model was fit to the delay time τ_{docking} between docking and fusion assuming different integer numbers between $N = 2\text{–}5$. To estimate the quality of the fit for each N, the corresponding reduced evaluated χ^2 values were compared resulting in the lowest χ^2 values for $N = 4$, which was then used to evaluate all the data (Fig. SI 12).
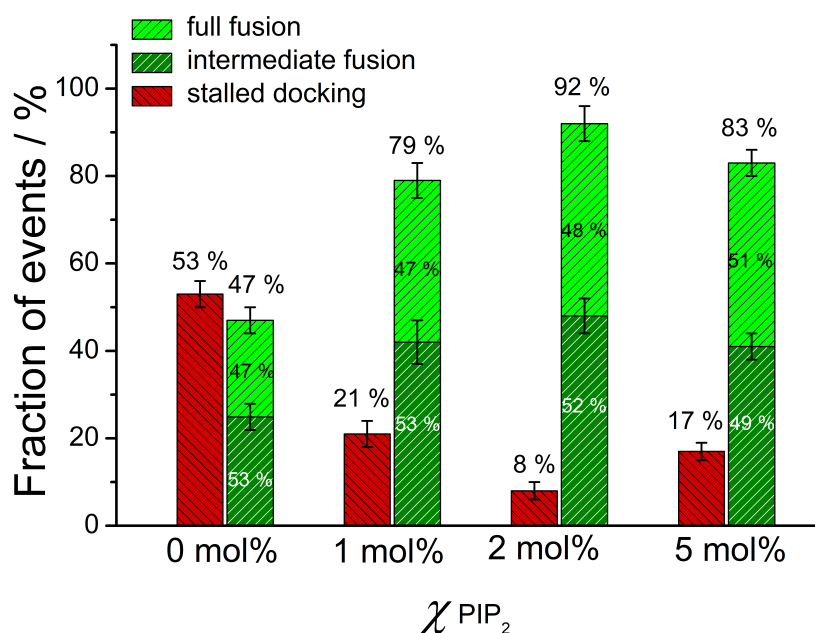
Fig. SI 13: Statistical analysis of the fusion efficiency of proteo-LUVs (DOPC/POPE/POPS/Chol/TexasRed-DPPE, 50:19:10:20:1) doped with syb 2 (p/l = 1:500) docked to PSMs dependent on the PI(4,5)P$_2$ content: DOPC/POPE/POPS/Chol/PI(4,5)P$_2$/Atto488-DPPE (50-x:19:10:20:x:1); $x = 0$ mol% ($n = 2043$, $m = 46$), 1 mol% ($n = 537$, $m = 27$), 2 mol% ($n = 994$, $m = 23$), 5 mol% ($n = 677$, $m = 25$) doped with the ΔN49-complex (p/l = 1:500) in the absence of Ca^{2+} (0.1 mM EGTA). The standard deviation of the mean values of each fusion state is depicted as error bar.

Supplementary Methods

Protein expression and isolation.

His$_6$-tagged SNAREs including full length synaptobrevin 2 (syb 2, aa 1-116), a soluble synaptobrevin 2 fragment (aa 49-96), syntaxin 1A (syx-1, aa 183-288), SNAP 25a (aa 1-206 with all cysteines replaced by serine) were recombinantly expressed in *E. coli* BL21(DE3) carrying a pET28a expression vector as described previously.[10,11] First purification of the SNAREs was performed by Ni-NTA agarose affinity chromatography. For syx-1 and full length syb 2, purification was achieved in the presence of 16 mM CHAPS. His$_6$-tags were then cleaved by thrombin overnight. Afterwards, thrombin was removed and the proteins were concentrated by ion exchange chromatography on MonoQ or MonoS columns (Äkta purifying system, GE Healthcare). The ΔN49-complex was assembled by first mixing syx-1 and the soluble syb 2 fragment (1:2) for 30 min, and then adding SNAP 25a (1:2:2) at 4°C. After overnight incubation at 4°C, the assembled complex was purified by ion exchange chromatography on a MonoQ column in the presence of 16 mM CHAPS. The success of ΔN49-complex formation was verified by SDS PAGE.[12,13] N-terminally His$_6$-tagged synaptotagmin-1 (syt-1, aa 1-421) was recombinantly expressed in *E. coli* strain BL21-CodonPlus (DE3)-RIPL. The purification was based on the general protocol of the SNAREs in the presence of 16 mM CHAPS.[10,11] After purification by Ni-NTA agarose affinity chromatography, the His$_6$-tag was removed by thrombin cleavage. Further purification and concentration of syt-1 was achieved by ion exchange chromatography using a MonoS column. Purity of the protein was verified by SDS PAGE.

Protein reconstitution into vesicles.

Syb 2 and syt-1 as well as the ΔN49-complex were reconstituted into small unilamellar vesicles (SUVs) by co-micellization in the presence of n-octyl-β-D-glycoside (n-OG) and subsequent detergent removal by size exclusion chromatography as described previously.[14]

Lipids dissolved in $CHCl_3$ (except for $PI(4,5)P_2$, which was dissolved in $MeOH/CHCl_3/H_2O$, 2:1:0.8) were mixed and the solvent was removed by an N_2 stream at 30°C followed by vacuum for 30 min at 30°C. The lipid films (0.5 mg) were solubilized in 50 μL HEPES buffer (20 mM HEPES, 100 mM KCl, 0.1 mM EGTA, 1 mM DTT, pH 7.4) containing 75 mM n-OG and proteins were added at the desired protein-to-lipid (p/l) ratio. After incubation of the mixed micelle solution for 30 min at room temperature, n-OG was removed via size exclusion chromatography (illustra NAP-25 G25 column, GE Healthcare). These vesicles were used to coat the silica beads and prepare the solid supported membranes.

For the co-reconstitution of syt-1 and and syb 2 in large unilamellar vesicles (LUVs), first LUVs were prepared by the extrusion method (400 nm nominal pore diameter) in HEPES buffer, which were then destabilized with 26 mM n-OG. Protein solutions were added to obtain the required p/l ratio and incubated for 30 min at room temperature. Size exclusion chromatography (illustra NAP-25 G25 column, GE Healthcare) in H_2O/buffer (9:1) was used to remove the detergent, the vesicle suspension was concentrated (Concentrator 5301, Eppendorf, Hamburg, Germany) and then transferred to a dialysis cassette (Slide-Analyzer, 0.1-0.5 mL, MWCO = 3.5 kDa, Thermo Fisher Scientific, Waltham, MA, USA) and dialyzed against HEPES buffer in the presence of Biobeads overnight at 4°C. A second size exclusion chromatography in HEPES buffer was used to remove residual detergent. Co-reconstitution of syt-1 and syb 2 was verified by Nycodenz density gradient centrifugation followed by SDS PAGE of the different fractions (Fig. SI 14).

For the preparation of giant unilamellar vesicles (GUVs) containing the $\Delta N49$-complex as used for the PSM-based fusion assay, a second size exclusion chromatography was performed in ultrapure H_2O to remove remaining detergent and salt. The proteoliposome suspension was then dried on indium tin oxide (ITO) slides in a desiccator over saturated NaCl solution. Electroformation was carried out by applying a sinusoidal voltage for 3 h (1.6 $V_{peak-peak}$, 12 Hz) to the ITO slides filled with 200 mM sucrose solution. GUVs were
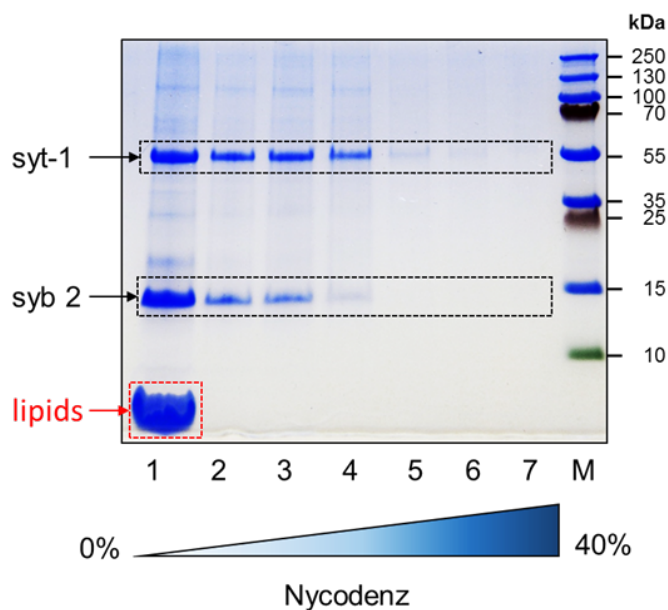
Fig. SI 14: Nycodenz assay to analyze the co-reconstitution of syt-1 (p/l = 1:1000) and syb 2 (p/l = 1:500) into LUVs. Fractions (1–7) were taken from top down after ultra-centrifugation of the syb 2/syt-1/LUV-suspension in a Nycodenz gradient (0–40% (w/v)) to separate proteoliposomes from unreconstituted protein. SDS-PAGE analysis of the samples (1–7) verified successful co-reconstitution of syt-1 and syb 2 into LUVs by showing the most prominent bands in fraction 1 with the lowest Nycodenz density and highest lipid content. M: marker.

harvested in fractions of 600 μL and inspected by wide field fluorescence microscopy to choose the fraction with the highest purity and amount of GUVs. Fusion activity of the SUVs or LUVs doped with syb 2 and syt-1 was monitored using SUVs or GUVs containing the ΔN49-complex using a lipid mixing assay based on FRET.[11]

Preparation of membrane–coated beads and solid supported membranes.

For the TPM experiments, membrane-coated silica beads were produced according to a protocol of Bao *et al.*[15] Silica beads (10 μL, 10 wt %, 0.96 μm) were incubated in a mixture of TRIS buffer (250 μL, 10 mM TRIS, 300 mM NaCl, pH 7.4) and the SUV suspension (250 μL) and pulse-vortexed in a centrifuge tube for 30 min to form continuous supported bilayers around the silica beads. Excess SUVs were removed by suspending the beads five times in 1 mL buffer followed by centrifugation for 5 s using a mini-centrifuge (LMS, Heidelberg,

Germany) at 6000 rpm and removing the supernatant. Solid supported membranes were generated by spreading SUVs on glass in HEPES buffer (20 mM HEPES, 150 mM KCl, pH 7.4).

Preparation of membrane-coated colloidal probe cantilevers.

Colloidal probe cantilevers were prepared by attaching a borosilicate glass microsphere with a diameter of 15 µm (Duke borosilicate glass 9015, Duke Scientific Corporation, Palo Alto, CA, USA) to a tipless MLCT-O10 cantilever (Bruker AFM Probes, Camarillo, CA, USA) using epoxy resin at a temperature of above 110 °C (Epikote 1004, Brenntag GmbH, Mühlheim, Germany 24). In detail, we used an upright light microscope (Olympus BX 51, Hamburg, Germany) with a $20\times$ magnification equipped with a nanomanipulator (MM3A-LS, Kleindiek Nanotechnik GmbH, Reutlingen, Germany). Before bilayer preparation on the colloidal probe the cantilevers were cleaned in an argon plasma for 30 s. The colloidal probe cantilever was then mounted in the AFM and incubated in proteoliposome solution ($80 - 100\ \mu$L, 3 mM in HEPES buffer (20 mM HEPES, 150 mM KCl, pH 7.4)) in a hanging droplet for at least 15 min at room temperature. Excess vesicle solution was removed by rinsing with HEPES buffer. The preparation was done immediately before carrying out force measurements. Force distance measurements were obtained using an MFP3D (Asylum Research, Santa Barbara, CA, USA). The cantilevers' spring constants were calibrated using the thermal noise method and were found to be in a range of 6-12 pN/nm. The colloidal probes were functionalized with PC-membranes doped with syt-1 (p/l = 1:100) to probe the interaction forces with a planar target membrane containing PS (11 mol%) and PI(4,5)P_2 if not indicated otherwise (Fig. 3). The high protein to lipid ratio ensures that enough syt-1 molecules (1-2) exist in the contact zone to show single rupture events in >50% of all force curves.

Tethered particle motion assay on solid-supported membranes.

Experiments were performed in a temperature-controlled, integrated flow chamber provided by the LUMICKS AFS^{TM} (stand-alone G2 system) or in a 6 channel μ-slide suitable for flow experiments (Ibidi, μ-slide VI 0.5, glass-bottom). A fiber-coupled collimated red LED (Thorlabs, M455F1, 685 nm) was coupled into the imaging path for illumination. A $60\times$ microscope objective (Nikon, CFI Plan Fluor $60\times$, NA 0.80) was used to image the illuminated membrane coated microspheres. 5-6 μL of the bead suspension (0.5 wt % beads) were added to capture about 10 microspheres/image section (900×900 pixel^2). Images were obtained with a CMOS-camera (UI324xCP-M, 1.280×1.024 pixels; Thorlabs) with a frame rate of 200 fps and an exposure time of 4.97 ms.

The tracking software is implemented in the standalone LUMICKS system. Acquired images were processed in real-time to extract the bead positions in three dimensions. A previously assigned template selects the diffraction pattern of the beads for a region of interest (ROI) of 65 pixels. Algorithms for determining the bead's position are based on cross-correlation (XCOR) and quadrant interpolation (QI). Before measuring the z-dimension, a lookup table (LUT) was made. Data analysis was performed with open source scientific tools in python (SciPy, Trackpy, Ruptures, Seaborn, Matplotlib, and Numpy) to analyze recorded bead trajectories, calculate MSDs, detect rupture forces, and for graphical illustration.

From holographic video particle tracking (HVPT), we collected x-, y-, and z-positions. First, each trajectory is smoothed with a Savitzky–Golay filter to average away particle localization errors and to generate a one-dimensional distance axis. Then, we performed a principal component analysis (PCA) from the `sklearn.decomposition` module for a linear dimensionality reduction using singular value decomposition (SDV) to project it to a lower-dimensional space. Following a transformation of data into a linear superposition of orthogonal components, arranged such that the first principal component has the largest

possible variance, i.e., it accounts for the largest contribution to the data variation. It divides the data set into main and conjugated components for a chosen number of components of two. Each component is then analyzed by the Pruned Exact Linear Time (PELT) method to search for change points in the bead's motion pattern equivalent to binding and unbinding events of single tethers or of multiple tether formation. PCA-analysis-PELT-segments are persistent for bond lifetimes. Afterward, each segment is characterized by its mean square displacement in two dimensions and its position fluctuation Δx. Confinement radii r_{conf} and characteristic confinement times τ are then extracted by fitting $\langle r^2 \rangle_{\text{conf}} = r_{\text{conf}}^2 \cdot \left(1 - e^{-\frac{t}{\tau}} \right)$ via non-linear least-squares minimization. The diffusion constant can be deduced from the characteristic time τ.

Atomic force microscopy - colloidal probe force spectroscopy.

All force distance cycles were operated with a forward velocity of 500 nm/s, varying retraction velocity and contact time (3 s and 10 s) at a loading force of 200 pN. Data were acquired in force volume mode to always address a new spot on the target membrane. More than $m > 10$ force maps with $n > 50$ individual force curves were acquired per category (lipid composition) and experiment ($k > 3$). We also collected data at different retraction velocity (100 - 5000 nm/s), and as typical for conventional slip bonds, we find an increase in rupture forces with speed. The measurements were performed in HEPES buffer with and without 1 mM $CaCl_2$. For each set of parameters at least 20×20 force-distance cycles over an area of $20 \times 20 \, \mu m^2$ were performed.

Single vesicle fusion assay on pore-spanning membranes.

For the preparation of pore-spanning membranes (PSMs) porous Si_3N_4 substrates with pore diameters of 1.2 μm (fluXXion, Eindhoven, The Netherlands) and 5 μm (Aquamarijn, Zutphen, The Netherlands) were used. The pores were 800 nm deep and open on both

sides. They were cleaned with ethanol followed by argon plasma (Zepto plasma cleaner, Diener Electronic, Ebbhausen, Germany). For surface functionalization, a thin layer of titanium was applied by sputter coating (Cressington Sputter Coater 108auto, Watford, UK) followed by a thermally evaporated 30-40 nm thick gold layer (MED020 coating system, Bal-Tec, Leica, Wetzlar, Germany) on top of the porous substrates. The gold coated substrates were incubated in 6-mercapto-1-hexanol (6 MH, $c = 1$ mM in n-propanol, overnight at 4°C). After rinsing with ethanol and ultrapure water, HEPES buffer (20 mM HEPES, 100 mM KCl, 0.1 mM EGTA, 1 mM DTT, pH 7.4) was added followed by the GUV suspension (10-20 μL) in isoosmolar sucrose solution. PSMs are formed due to spontaneous rupture of GUVs that adhere to the hydrophilic surface of the porous substrate. Residual lipid material as well as non-spread GUVs were removed by buffer exchange.

For single vesicle fusion recordings, an upright confocal laser scanning microscope (LSM 710, Zeiss, Jena, Germany) equipped with a water immersion objective WPlan-APOCHROMAT (63×, NA 1.0, Zeiss, Jena, Germany) was used. By utilizing a spectral detector (photo-multiplier tube, PMT), two channel recordings (Atto488-DPPE, λ_{ex} = 488 nm, λ_{em} = 495-545 nm and TexasRed-DPPE, λ_{ex} = 561 nm, λ_{em} = 610-700 nm) were performed. The vesicle assay was started by injecting 0.5-1.0 μL proteoliposome suspension onto the PSM patch in the focal plane. Time series of 2500 images with a frame rate of 8 Hz, a resolution of 256×256 pixel^2 and a color depth of 16 bit were recorded. The area of the imaged PSM patch was 40×40 μm^2 and the detector pinhole was adjusted to a diameter of 300 nm. Time resolved fluorescence intensities from both channels (Atto488 and TexasRed) were read out to detect single vesicle fusion events. A threshold based localization of docked vesicles was performed followed by placing a region of interest (ROI) of 2×2 - 5×5 pixel^2 on the center of mass of the docked vesicles and reading out the fluorescence intensities of both channels within this ROI.[11,16]

References

1. Visser, E. W. A.; van IJzendoorn, L. J.; Prins, M. W. J. Particle motion analysis reveals nanoscale bond characteristics and enhances dynamic range for biosensing. *ACS Nano* **2016**, *10*, 3093–3101.

2. Visser, E. W. A.; Yan, J.; van IJzendoorn, L. J.; Prins, M. W. J. Continuous biomarker monitoring by particle mobility sensing with single molecule resolution. *Nat. Commun.* **2018**, *9*, 2541.

3. Oelkers, M.; Witt, H.; Halder, P.; Jahn, R.; Janshoff, A. SNARE-mediated membrane fusion trajectories derived from force-clamp experiments. *Proc. Natl. Acad. Sci. U. S. A.* **2016**, *113*, 13051–13056.

4. Witt, H.; Savić, F.; Verbeek, S.; Dietz, J.; Tarantola, G.; Oelkers, M.; Geil, B.; Janshoff, A. Membrane fusion studied by colloidal probes. *Eur. Biophys. J.* **2021**, *50*, 1–15.

5. Abdulreda, M. H.; Moy, V. T. Investigation of SNARE-mediated membrane fusion mechanism using atomic force microscopy. *Jpn. J. Appl. Phys.* **2009**, *48*, 08JA03.

6. Bonaccurso, E.; Kappl, M.; Butt, H.-J. Hydrodynamic force measurements: Boundary slip of water on hydrophilic surfaces and electrokinetic effects. *Phys. Rev. Lett.* **2002**, *88*, 076103.

7. Jarzynski, C. Nonequilibrium equality for free energy differences. *Phys. Rev. Lett.* **1997**, *78*, 2690–2693.

8. Hummer, G.; Szabo, A. Free energy surfaces from single-molecule force spectroscopy. *Acc. Chem. Res.* **2005**, *38*, 504–513.

9. Floyd, D. L.; Ragains, J. R.; Skehel, J. J.; Harrison, S. C.; Van Oijen, A. M. Single-particle kinetics of influenza virus membrane fusion. *Proc. Natl. Acad. Sci. U. S. A.* **2008**, *105*, 15382–15387.

10. Hernandez, J. M.; Stein, A.; Behrmann, E.; Riedel, D.; Cypionka, A.; Farsi, Z.; Walla, P. J.; Raunser, S.; Jahn, R. Membrane fusion intermediates via directional and full assembly of the SNARE complex. *Science* **2012**, *336*, 1581–1584.

11. Schwenen, L. L. G.; Hubrich, R.; Milovanovic, D.; Geil, B.; Yang, J.; Kros, A.; Jahn, R.; Steinem, C. Resolving single membrane fusion events on planar pore-spanning membranes. *Sci. Rep.* **2015**, *5*, 12006.

12. Schägger, H.; Jagow, G. v. Tricine-sodium dodecyl sulfate-polyacrylamide gel electrophoresis for the separation of proteins in the range from 1 to 100 kDa. *Anal. Biochem.* **1987**, *166*, 368–379.

13. Schägger, H. Tricine-SDS-PAGE. *Nat. Protoc.* **2006**, *1*, 16–22.

14. Pobbati, A. V.; Stein, A.; Fasshauer, D. N- to C-terminal SNARE complex assembly promotes rapid membrane fusion. *Science* **2006**, *313*, 673–676.

15. Bao, C.; Pähler, G.; Geil, B.; Janshoff, A. Optical fusion assay based on membrane-coated spheres in a 2D assembly. *J. Am. Chem. Soc.* **2013**, *135*, 12176–12179.

16. Kuhlmann, J. W.; Junius, M.; Diederichsen, U.; Steinem, C. SNARE-mediated single-vesicle fusion events with supported and freestanding lipid membranes. *Biophys. J.* **2017**, *112*, 2348–2356.